



**HAL**  
open science

## In-Ground-Effect Disturbance-Rejection Altitude Control for Multi-Rotor UAVs

Juan Díaz-Téllez, J. Fermi Guerrero-Castellanos, Florian Pouthier, Nicolas Marchand, Sylvain Durand

► **To cite this version:**

Juan Díaz-Téllez, J. Fermi Guerrero-Castellanos, Florian Pouthier, Nicolas Marchand, Sylvain Durand. In-Ground-Effect Disturbance-Rejection Altitude Control for Multi-Rotor UAVs. *Journal of Intelligent and Robotic Systems*, 2023, 109 (2), pp.27. 10.1007/s10846-023-01958-4 . hal-04220371

**HAL Id: hal-04220371**

**<https://hal.science/hal-04220371v1>**

Submitted on 27 Sep 2023

**HAL** is a multi-disciplinary open access archive for the deposit and dissemination of scientific research documents, whether they are published or not. The documents may come from teaching and research institutions in France or abroad, or from public or private research centers.

L'archive ouverte pluridisciplinaire **HAL**, est destinée au dépôt et à la diffusion de documents scientifiques de niveau recherche, publiés ou non, émanant des établissements d'enseignement et de recherche français ou étrangers, des laboratoires publics ou privés.



Distributed under a Creative Commons Attribution - NonCommercial - ShareAlike 4.0 International License

# In-Ground-Effect Disturbance-Rejection Altitude Control for multi-rotor UAVs

J. Díaz-Téllez<sup>1,2</sup>, J.F. Guerrero-Castellanos<sup>1\*</sup>, F.  
Pouthier<sup>3</sup>, N. Marchand<sup>3</sup> and S. Durand<sup>4</sup>

<sup>1</sup>Facultad de Ciencias de la Electrónica, Benemérita Universidad  
Autónoma de Puebla, Puebla, 72570, Puebla, Mexico.

<sup>2</sup>Departamento Eléctrica-Electrónica, TecNM/Instituto  
Tecnológico de Puebla, Mexico, Puebla, 72220, Puebla, Mexico.

<sup>3</sup>Univ. Grenoble Alpes, CNRS, Grenoble INP, GIPSA-lab, 38000,  
Grenoble, France.

<sup>4</sup>ICube Laboratory, CNRS, INSA, Strasbourg University, 67000,  
Strasbourg, France.

\*Corresponding author(s). E-mail(s):

[fermi.guerrero@correo.buap.mx](mailto:fermi.guerrero@correo.buap.mx);

Contributing authors: [juan.diaz@puebla.tecnm.mx](mailto:juan.diaz@puebla.tecnm.mx);

[Florian.Pouthier@gipsa-lab.fr](mailto:Florian.Pouthier@gipsa-lab.fr); [nicolas.marchand@gipsa-lab.fr](mailto:nicolas.marchand@gipsa-lab.fr);

[sdurand@unistra.fr](mailto:sdurand@unistra.fr);

## Abstract

This paper presents a robust altitude control that merges the principles of active disturbance rejection control (ADRC) with the in-ground-effect model (IGE). To this end, a nonlinear extended state observer is designed along the vertical axis, taking attitude and altitude measurements. Then, the forces generated by low-level flight, ground effect and other external disturbances are estimated and used (as an anticipation term) together with a non-linear control law (as a feedback term) to reject them. Closed-loop stability is analyzed in the Lyapunov sense. Extensive numerical simulations and real-time experiments validate the proposal. Thanks to its simplicity, the control algorithm is easy to implement. It can be used for various maneuvers that depend on proximity to the ground, obstacles or surfaces, such as take-off, landing, inspection, surveillance and hovering.

**Keywords:** In-Ground-Effect Control, ADRC, Extended State Observer, multi-rotor-UAV, Low Altitude, Wind Gust.

## 1 Introduction

The VTOL-UAV multicopter has rapidly become a standard platform for the study of aerial robotics. This aircraft is used to analyze aerodynamic effects, modeling, control algorithms, trajectory planning and autonomous navigation. It has interesting properties from a control theory point of view: it is non-linear with a multiple inputs and outputs (MIMO system), under-actuated, subject to external disturbances and various aerodynamic effects.

This type of vehicle has been used for inspection [1, 2], delivery services [3], precision agriculture [4–6], pollution monitoring [7, 8], and search and rescue operations [9, 10] to name a few. In [11, 12], the authors present a really nice survey of the applications and control techniques used in multi-rotor UAVs. Most of the applications mentioned above require an approach to the object of study in addition to the interaction with its environment.

In these applications, UAVs are expected to perform maneuvers near the ground, rigid surfaces, or obstacles. The ground effect modifies aerodynamic drag generated by the wings or propellers of an aircraft when it is close to a fixed surface. This effect is the consequence of the distortion of the airflow due to the proximity of the ground or rigid surfaces [13]. Mathematical models have been proposed to describe the ground effect in hover and forward flight. These models are essential for developing robust controls for applications such as landing, hovering and low-altitude flight, and motion planners for energy-saving applications. Ground effect has been studied in helicopters for years. A practical method describing the helicopter ground effect was proposed in [14]. This model describes the thrust-in-ground effect (IGE) and the outside-of-ground effect (OGE) as a function of the rotor radius, vertical distance and forward velocity. Similarly, the work in [15] obtains a ground effect model for a single rotor in hovering flight by experimentation. Unfortunately, it has been shown that these models do not accurately describe the multi-rotor ground effect [16–18]. In [19], the authors use visual feedback to model the ground effect forces experienced by a multi-rotor. The work in [18] proposes a ground effect model using the Draganflyer X8, actuated by eight propellers arranged in four coaxial pairs in a quadrotor configuration. In this analysis, it is shown that the ground effect is more substantial than that predicted in [14].

In [16], a ground effect compensator based on the Cheeseman model [14] with a correction coefficient is proposed. More recently, in [20], the influence of the ground effect on the lateral movement of the multi-rotor is analyzed. The force generated by the ground effect modeled as a spring is integrated into the thrust of the rotors. In [17], the authors present two effective data-driven models that describe the ground effect in hover and in forward flight. Extensive tests under different conditions validate their proposed models.

**Table 1** Main IGE models.

Authors	Model	Multi-rotor	Forward Flight
Cheeseman [14]	$\frac{T_{IGE}}{T_{OGE}} = \frac{1}{1 - \frac{(r/4z_r)^2}{1 + (V/v_i)^2}}$	No	Yes
Hayden [15]	$\frac{T_{IGE}}{T_{OGE}} = \left(0.9926 + \frac{0.03794}{(z/2r)^2}\right)^{2/3}$	No	No
Danjun [16]	$\frac{T_{output}}{T_{input}} = \frac{1}{1 - \rho \left(\frac{r}{4z_r}\right)^2}$	Yes	No
Kan [17]	$\frac{T_{IGE}}{T_h} = \frac{1 - \frac{3r}{25z}}{1 + \frac{3}{50} \left(\frac{V}{v_h}\right)^3}$	Yes	Yes

Some IGE models reported in the literature.

Most ground effect models depend on the propeller's radius  $r$  and the altitude  $z_r$  measured to the ground in the hover condition. In forwarding flight conditions, a dependency on the multi-rotor's longitudinal speed is added. Table 1 summarizes the properties of the literature's most widely used ground effect models. Despite the significant development of IGE models, there has been very little progress in designing altitude controllers that use these models as part of the control law [21].

Low-altitude flights with multi-rotor vehicles are a challenge from an automatic control perspective. The ground effect, forces, and moments due to the crosswind generated by the flat surfaces cause degradation in the position and attitude control systems. Consequently, they are prone to fatal accidents. Nowadays, extensive research has been carried out on controller design for altitude stabilization as part of position controllers; remarkable work on the subject can be found in [22–26]. However, none of the works cited above implicitly addresses the problem of ground effect and external disturbances.

Recently, various control strategies have been proposed to deal explicitly with different aerodynamic effects and external disturbances [27–29]. In [30], the authors propose an excellent work to compensate for the aerodynamic effects on multi-rotor UAVs through a control allocation approach using neural networks by replacing the classic so-called mixing matrix. In [31], a robust altitude controller based on one-step-ahead predictive is proposed. Simulations are carried out against low-frequency disturbances and payload variations. However, no physical tests are performed to check the controller's robustness. Environmental disturbances such as wind gusts greatly influence trajectory control design and route planning; dealing with constant gusts of wind is very common in outdoor. In urban environment the UAV may deviate from the desired path [32]. Research has been done on the subject in [32–35]. In [35] a frequency-based nonlinear disturbance observer (NDOB) for estimating wind gusts is proposed. The NDOB considers the frequency range of the wind gust, isolating other disturbances and focusing on the wind. Nevertheless, they only address the estimation without focusing on a robust control that allows mitigating

these disturbances. In [36], sliding mode-based controllers are implemented to control the position of a multi-rotor UAV in real-time. The three evaluated control algorithms are based on the second-order sliding mode technique [37]. The results show that these algorithms are robust to external disturbances, noise, and parametric variations, in addition to reducing the chattering phenomenon. The analysis based on the error's dynamics shows that the Modified Super Twisting Sliding Mode Controller (MST-SMC) presents better performance. However, low-altitude flights are not performed. In [38], a sliding mode control-based is designed for altitude and attitude at low-altitude flight operation, compensating for wind disturbance with a maximum speed of 3.3 m/s. Automatic take-off and landing maneuvers are carried out practically. However, this work does not address the ground effect; the ground clearance is not low enough to produce this aerodynamic effect. In [39] a safety control is proposed based on a proportional-derivative (PD) controller to stabilize the position, and a sliding mode controller (SMC) to stabilize the attitude; a disturbance observer is integrated to deal with ground effect and blade damage. The control law can follow a circular path close to a surface, simultaneously experiencing ground effect and blade damage. In [40] a nonlinear disturbance control and an observer are designed to compensate for the impact of the ground effect. Adaptive control based on ground effect models is designed to operate at low altitudes where the ground effect is high and is addressed in [21]. Tests show that the algorithm can tune the ground effect at a low altitude and in the autonomous landing task. However, the design does not take into account external disturbances. Anti-disturbance control has been a practical methodology for developing robust algorithms for parametric uncertainties, faults, and external disturbances. Since the seminal work of Han [41], Active Disturbance Rejection Control (ADRC) has become essential to the design of control algorithms that allow online estimation of disturbances caused by unknown system dynamics and exogenous disturbances. The total disturbance is estimated by an Extended State Observer (ESO) [42–44] so-called disturbance-observer [45] and then “rejected” by way of combination of feedback (in general linear) and feed-forward terms [46, 47]. This approach has many practical advantages since it does not use trained methods and does not require additional sensors and complex instrumentation. The ADRC technique has been exploited in numerous works for position control of multi-rotor aerial vehicles *e.g.*, [48–52] since it is very effective to reject external disturbances, including wind gusts and model uncertainties. These approaches use the classic structure of the ADRC; an extended state observer, to estimate the total disturbance and linear feedback control, except in [49, 53] where nonlinear feedback is used. However, to the authors' knowledge, it has not been used, together with IGE model, in the design of altitude controllers for multi-rotor UAVs subject to external disturbances.

The present paper aims to combine the ideology of ADRC design with the in-ground-effect model. The novelty of the proposed strategy lies in merging the qualities of the ADRC approach using an ESO to estimate the total

disturbance, a smooth nonlinear feedback control based on nested saturation functions, and a mathematical model describing the ground effect allowing adaptation to the input gain, which represents a critical point in the performance of the ADRC approach [54]. Stability analysis of the closed-loop system reveals practical asymptotic stability to the origin of the state-space error. Extensive simulations and real-time experiments are performed to show the closed-loop robustness to external disturbances (wind gusts) and the capabilities to fly to very low altitudes. A comparison regarding a nonlinear controller, namely the MST-SMC, was performed, showing the advantages of the proposed approach.

This paper is structured as follows. Section 2 presents the mathematical model of the aircraft and the influences of the ground effect and wind gust disturbance. Section 3 is devoted to the design of the proposed control scheme. Section 4 deals with numerical simulations where the rejection capabilities towards external disturbances in hovering flight and waypoint regulation at low altitude flight is presented and discussed. In Section 5, experimental flights are performed, and the results are presented. Finally, Section 6 presents the conclusions and future work.

## 2 Mathematical Model

The multicopter can be modeled as a rigid body with six degrees of freedom sub-actuated with only four independent control inputs: three moments in their respective axes and one thrust force perpendicular to the aircraft. For convenience, two reference frames are introduced to study the dynamics of this aircraft and determine its position. The inertial frame  $\{I\} = [e_1^I \ e_2^I \ e_3^I]$  and the body frame  $\{B\} = [e_1^B \ e_2^B \ e_3^B]$  is fixed to the multi-rotor. Figure 1 shows the relationship between both frames of reference, both obey the right hand law. Some assumptions are made to model the multi-rotor:

- The aircraft is a rigid body.
- The structure is supposed symmetrical.
- The centre of gravity and the geometric center are assumed to coincide.

### 2.1 Motion Equations of multi-rotor UAVs

Based on Euler's theorem, the rotation of the multi-rotor can be achieved by three elementary rotations about a fixed point of the inertial frame. The rotation of the coordinates of a point from body frame  $\{B\}$  with respect to inertial frame  $\{I\}$  is represented by the orthogonal rotation matrix  $R \in SO(3) = \{R \in \mathbb{R}^{3 \times 3} : R^T R = I_3, \det(R) = 1\}$ , where  $I_3 \in \mathbb{R}^{3 \times 3}$  is the identity matrix. Euler angles (roll,pitch,yaw) is a representation of attitude that can be obtained using the vector  $\Theta = [\phi \ \theta \ \psi]^T$ . The corresponding rotation matrix

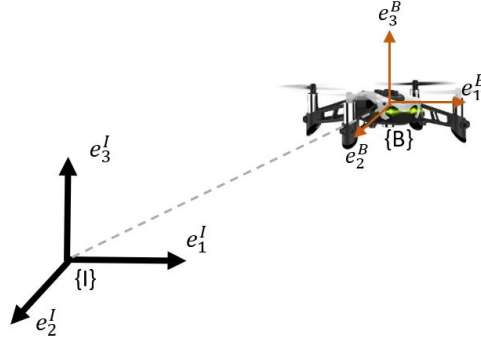


**Fig. 1** Relationship between the  $\mathbf{E}^f$  and  $\mathbf{E}^b$  Coordinate Frames.

is then given through the map  $R : \mathbb{R}^3 \rightarrow SO(3)$  by:

$$R = \begin{bmatrix} \cos \psi \cos \theta & \cos \phi \sin \theta \sin \phi - \sin \psi \cos \phi & \cos \psi \sin \theta \cos \phi + \sin \psi \sin \phi \\ \cos \theta \cos \psi & \sin \phi \sin \theta \sin \phi + \cos \psi \cos \phi & \sin \psi \sin \theta \cos \phi - \cos \psi \sin \phi \\ -\sin \theta & \sin \phi \cos \theta & \cos \phi \cos \theta \end{bmatrix} \quad (1)$$

**Remark 1** In this paper,  $R_B^I = R$  is the matrix that rotates the coordinates of a point from  $\{B\}$  to  $\{I\}$ .

The position of the center of the mass of the multi-rotor is given by the vector  $p = [x \ y \ z]^T$  and is defined in the inertial coordinate system  $\{I\}$ . The translational velocities  $v = [v_x \ v_y \ v_z]^T$  can be related to the derivative with respect to time of the position as shown in Equation (3). The angular velocities  $\omega = [\omega_x \ \omega_y \ \omega_z]^T$  measurement in the body coordinate frame  $\{B\}$ , relative to the inertial coordinate frame  $\{I\}$ . The attitude matrix (2) relates the attitude rate  $\dot{\Theta}$  to the angular velocity  $\omega$  of the multi-rotor.

$$W = \begin{bmatrix} 1 & \sin \phi \tan \theta & \cos \phi \tan \theta \\ 0 & \cos \phi & -\sin \phi \\ 0 & -\sin \phi / \cos \theta & \cos \phi / \cos \theta \end{bmatrix} \quad (2)$$

Using Newton's second law, it follows:

$$\Sigma_T : \begin{cases} \dot{p} = v \\ \dot{v} = \frac{1}{m} R e_3^B T - g e_3^I + \xi_T(t) \end{cases} \quad (3)$$

$$\Sigma_R : \begin{cases} \dot{\Theta} = W \omega \\ J \dot{\omega} = -[\omega^\times] J \omega + \tau + \xi_R(t) \end{cases} \quad (4)$$

where  $\Sigma_T$  and  $\Sigma_R$  represent the translation and rotation dynamics, respectively.  $m$  stands for the mass of the VTOL-UAV, and  $J$  for the inertial

matrix.  $g$  ( $m \cdot s^{-2}$ ) represents the gravity acceleration. The total thrust  $e_3^B T$  is expressed in  $\{B\}$ . Uncertainties, malfunctions of some components, external disturbances and aerodynamic effects that induce forces and torques on the aircraft are considered in the terms  $\xi_T$  and  $\xi_R$ . The  $\xi_T(t) = [\xi_x \ \xi_y \ \xi_z]^T$  includes the effect of the wind gusts dynamics  $F_w$ , ground effect  $F_{GE}$  and unmodeled dynamics, noise and external disturbance  $\zeta(t)$ . The total disturbance can be expressed as in Equation (5).

$$\xi_T(t) = F_w + F_{GE} + \zeta(t). \quad (5)$$

Similarly for  $\xi_R(t) = [\xi_{Rx} \ \xi_{Ry} \ \xi_{Rz}]^T$  represents an additive time-varying perturbation, produced by wind  $\tau_w$ , ground effect  $\tau_{GE}$  and gyroscopic torques  $\zeta_r(t)$  due to the rotation of the propellers.

$$\xi_R(t) = \tau_w + \tau_{GE} + \zeta_r(t). \quad (6)$$

This conglomeration of disturbances largely dependent on the states of the system is necessary for an accurate description of the multi-rotor. In this investigation, we focus on designing a robust control law that allows the multi-rotor to operate near the ground or rigid surfaces. The motivation behind this approach involves current applications of multi-rotor UAVs, such as package delivery, data collection, generation of energy-efficient trajectories, and interaction with other aircraft in cooperative tasks.

## 2.2 Ground-Effect Model

It is well known that the ground effect reduces the aerodynamic drag generated by the wings or propellers of an aircraft when it is close to a fixed surface; that is, it produces more thrust close to a surface than when flying at a great distance from any surface. The model used in Section 3 to design the altitude controller is the one proposed by [16]. This model was previously analyzed in [13]. According to experimental results presented in Appendix B, it is the one that has the best behavior for our application. This model introduces a correction coefficient to the well-known Cheeseman model and is the following

$$\frac{T_{output}}{T_{input}} = \frac{1}{1 - \rho \left( \frac{r}{4z_r} \right)^2} \quad (7)$$

where  $r$  is the radius of the propeller,  $z_r = z + 0.02$  m is the vertical distance from the rotor to the ground,  $\rho$  is a positive coefficient which is determined experimentally (see Appendix A).  $T_{input}$  is the input thrust commanded by the flight controller, *i.e.*, the thrust calculated by the control law, and  $T_{output}$  is the actually thrust generated by the aircraft's actuators.

## 2.3 Problem Statement

The main objective of the present work is to design a precise altitude robust control for a multi-rotor subject to external disturbances, ground effect dynamics, and parametric uncertainties. The purpose of the altitude controller is to stabilize the aircraft at a desired reference position  $z_d$ , sufficiently close to the ground, with the desired velocity  $v_{zd}(t) = 0$ :

$$z(t) \rightarrow z_d(t), \quad v_z \rightarrow v_{zd}(t) = 0, \quad \text{as } t \rightarrow \infty. \quad (8)$$

**Assumption 1** *The disturbance function  $\xi_z$  is uniformly absolutely bounded, i.e.  $\|\xi_z(t)\|_\infty \leq \xi_z$ .*

## 3 An Active Disturbance Rejection Control with a Ground-Effect Model

This section describes the structure and design of the proposed control algorithm for the multi-rotor. Most of the time, the controller is based on a cascade structure; the outer loop controller (dynamics of position) and the inner loop controller (attitude dynamic). The outer loop control calculates the desired angles  $\Theta_d(t)$  and the desired thrust  $f_d(t)$  according to the desired trajectory position  $p_d(t)$  of the UAV. The inner loop control computes the desired moments  $\tau_d(t)$  according to the desired angles  $\Theta_d$ . Furthermore, the outer controller can be broken into two subsystems: altitude and horizontal position control. In this work, we focus on altitude control. Therefore, it is assumed that the horizontal position is automatically regulated (and, consequently, the attitude).

### 3.1 Disturbance Estimation

In this section, an extended-state nonlinear observer (ESO) is designed on the vertical axis by taking measurements of the Euler angles, the desired thrust, and the nonlinear dynamics of the multi-rotor to estimate additive endogenous and exogenous disturbances such as wind gust effects.

Let us define the following variable,  $\Lambda(\phi, \theta) = \frac{\cos \phi \cos \theta}{m}$  which is assumed to be known. Then, the dynamics along the  $z$ -axis given by (3) can be rewritten as follows using the Danjun model (7):

$$\Sigma_z := \begin{cases} \dot{z} = v_z \\ \dot{v}_z = \Lambda(\phi, \theta)T_{output} + \xi_z(t) \\ \quad = \frac{\Lambda(\phi, \theta)}{1 - \rho\left(\frac{r}{4z_r}\right)^2}T_{input} + \xi_z(t) \end{cases} \quad (9)$$

For sake of simplicity, let  $T$  stand for  $T_{input}$  and  $\tilde{\Lambda}(\phi, \theta, z_r) := \frac{\Lambda(\phi, \theta)}{1 - \rho \left( \frac{r}{4z_r} \right)^2}$ . In order to estimate the endogenous and exogenous disturbances lumped in the term  $\xi_z$ , we introduce the following extended state observer (ESO):

$$\Sigma_{ESO} : \begin{cases} \dot{\hat{z}} = \hat{v}_z + l_2 (z - \hat{z}) \\ \dot{\hat{v}}_z = \tilde{\Lambda}(\phi, \theta, z_r) T + \hat{\xi}_z + l_1 (z - \hat{z}) \\ \dot{\hat{\xi}}_z = l_0 (z - \hat{z}) \end{cases} \quad (10)$$

where  $l_1, l_2$  and  $l_3$  are the observer's gains which are chosen such that the characteristic polynomial of the observer's error dynamics matches those of the desired polynomial  $P(\lambda) = \left( \lambda^2 + \frac{2\zeta\omega_n}{\epsilon} \lambda + \frac{\omega_n^2}{\epsilon^2} \right) (\lambda + \frac{p_0}{\epsilon})$ . Thus, one has

$$l_0 = \frac{1}{\epsilon^3} (\omega_n^2 p_0), \quad l_1 = \frac{1}{\epsilon^2} (2p_0 \zeta \omega_n + \omega_n^2), \quad l_2 = \frac{1}{\epsilon} (p_0 + 2\zeta \omega_n) \quad (11)$$

with  $\epsilon \in \mathbb{R}+$  sufficiently small and  $\omega_n, \zeta, p_0 \in \mathbb{R}+$ .

**Proposition 2** *The estimation error  $e = z - \hat{z}$  satisfies the following perturbed linear differential equation*

$$e^{(3)} + l_2 \ddot{e} + l_1 \dot{e} + l_0 e = \dot{\xi}_z(t)$$

*if the observer's gains are chosen as in Equation (11) with  $P$  chosen Hurwitz, the trajectories of the estimation error globally converge towards a sphere of radius  $\bar{\rho}$  with  $\bar{\rho}$  as small as desired, centered at the origin of the estimation error phase space  $\{e, \dot{e}, \ddot{e}\}$  where they remain ultimately bounded.*

*Proof* The proof follows the one presented in [46, 55]. □

**Remark 2** *Note that the observer (10) could estimate the gravity term  $g$  together with the perturbation  $\xi_z$  using only one lumped perturbation term  $\hat{\xi}_z$ .*

## 3.2 A Control Strategy with Active Disturbance Rejection and Ground-Effect Compensation

This section proposes a control law with active disturbance rejection and ground-effect compensation. It is based on nested saturation functions [56]. In that aim, we define:

**Definition 1** *Given a positive constant  $M$ , a continuous and non-decreasing function  $\sigma_M : \mathbb{R} \rightarrow \mathbb{R}$  is defined as:*

- (1)  $\sigma_M = s$  if  $|s| < M$
- (2)  $\sigma_M = M \cdot \text{sign}(s)$  else

Now, we are ready to give the control law.

**Proposition 3** *Consider system (9) with the following bounded control input*

$$T_{IGE-ADRC-NL} = -\tilde{\Lambda}^{-1}(\phi, \theta, z) \left( \hat{\xi}_z + \sigma_{M_2}(a_1 v_z + \sigma_{M_1}(a_2 v_z + a_1 a_2(z - z_d))) \right) \quad (12)$$

where  $\sigma_{M_1}$  and  $\sigma_{M_2}$  are saturation functions such that  $M_2 > 2M_1$ ,  $a_1, a_2 \in \mathbb{R}_+$  are tuning parameters.  $\hat{\xi}_z$  is the estimation of the unknown disturbance  $\xi_z$ . Then, the trajectories of the system converge towards a small sphere centered at the origin of the phase space  $\{z, v_z\}$  where they remain ultimately bounded.

*Proof* The closed-loop system becomes:

$$\begin{aligned} \dot{z} &= v_z \\ \dot{v}_z &= -\sigma_{M_2}(a_1 v_z + \sigma_{M_1}(a_2 v_z + a_1 a_2(z - z_d))) + \xi_z - \hat{\xi}_z \end{aligned} \quad (13)$$

Let us define the following linear transformation:

$$z_1 = a_1 a_2(z - z_d) + a_2 v_z; \quad z_2 = a_1 v_z, \quad \text{with, } a_1, a_2 \in \mathbb{R}_+$$

then, the closed-loop system (13) becomes:

$$\begin{aligned} \dot{z}_1 &= a_2 z_2 - a_2 \sigma_{M_2}(z_2 + \sigma_{M_1}(z_1)) + a_2 \tilde{\xi} \\ \dot{z}_2 &= -a_1 \sigma_{M_2}(z_2 + \sigma_{M_1}(z_1)) + a_1 \tilde{\xi} \end{aligned} \quad (14)$$

with  $\tilde{\xi} = \xi_z - \hat{\xi}_z$ . In order to analyse the closed-loop stability, we begin by considering the evolution of the state  $z_2$ . Consider the Lyapunov function  $V_2 = \frac{1}{2}z_2^2$ . The derivative of  $V_2$  is given by

$$\dot{V}_2 = -a_1 z_2 \sigma_{M_2}(z_2 + \sigma_{M_1}(z_1)) + a_1 z_2 \tilde{\xi} \quad (15)$$

Assuming that  $|z_2| > 2M_1$ , it follows that  $|z_2 + \sigma_{M_1}(z_1)| > M_1 + \varepsilon$ , with  $\varepsilon$  sufficiently small. Then,  $z_2 + \sigma_{M_1}(z_1)$  has the same sign than  $z_2$ . From Proposition 2,  $\tilde{\xi}$  remains bounded with bound denoted  $\bar{d}$ , then

$$\dot{V}_2 \leq -a_1 |z_2| \sigma_{M_2}(M_1 + \varepsilon) + a_1 |z_2| \bar{d} \quad (16)$$

assuming that  $\bar{d} < \min(M_2, (M_1 + \varepsilon))$ , one can ensure the decrease of  $V_2$ , i.e.,  $\dot{V}_2 < 0$ . Consequently,  $z_2$  enters the set  $\Phi_2 = \{z_2 : |z_2| \leq 2M_1\}$  in finite time  $t_1$  and remains in it thereafter. Therefore, (14) becomes

$$\begin{aligned} \dot{z}_1 &= -a_2 \sigma_{M_1}(z_1) + a_2 \tilde{\xi} \\ \dot{z}_2 &= -a_1(z_2 + \sigma_{M_1}(z_1)) + a_1 \tilde{\xi} \end{aligned} \quad (17)$$

now consider the evolution of  $z_1$ . For that, let  $V_1 = \frac{1}{2}z_1^2$  be a Lyapunov function. The derivative of  $V_1$  is given by

$$\begin{aligned} \dot{V}_1 &= -a_2 z_1 \sigma_{M_1}(z_1) + a_2 z_1 \tilde{\xi} \\ &\leq -a_2 |z_1| (M_1) + a_2 |z_1| \bar{d} \end{aligned} \quad (18)$$

assuming that  $\bar{d} < M_1$ , then  $\dot{V}_1 < 0$ . Consequently,  $z_1$  enters  $\Phi_1 = \{z_1 : |z_1| \leq M_1\}$  in finite time  $t_2$  and remains in it thereafter. Consequently, (14) becomes

$$\begin{aligned} \dot{z}_1 &= -a_2 z_1 + a_2 \tilde{\xi} \\ \dot{z}_2 &= -a_1 z_2 - a_1 z_1 + a_1 \tilde{\xi} \end{aligned} \quad (19)$$

Note that Equations (19) represent a stable perturbed linear system. Then, the trajectories of the system converge towards a small sphere of radius  $\bar{\rho}$  centered at the origin of the phase space  $\{z_1, z_2\}$  and, due to the linear transformation, of the phase space  $\{z, v_z\}$  where they remain ultimately bounded.  $\square$

Figure 2 shows the global block diagram of the proposed control strategy. This diagram shows the interaction between the extended state observer ESO, the bounded control and the ground effect compensator.

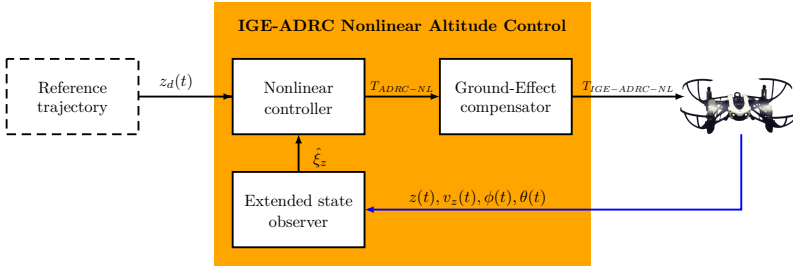


**Fig. 2** Block diagram of the robust altitude control.  $T_{ADRC-NL}$  is defined by Equation (22).

## 4 Numerical validation

In this section, numerical simulations are performed to validate the proposed approach considering the ground effect and forces induced by wind gusts.

The above control strategy, namely  $T_{IGE-ADRC-NL}$  of Equation (12), is compared with different control strategies derived removing the disturbance estimator (called  $T_{IGE-NL}$  in the sequel), or the ground effect compensation (called  $T_{ADRC-NL}$  in the sequel), or both (called  $T_{NL}$  in the sequel). Those control laws are formally defined in Equations (21), (22), and (20), respectively. In addition, a modified super twisting sliding mode strategy inspired by [36] has also been implemented for comparison with the proposed method. This control is called  $T_{MST-SMC}$  and is given in Equation (23). Classical performance indexes are used in all simulations and experiments: integral square error (ISE), integral time square error (ITSE), integral absolute error (IAE), and integral time absolute error (ITAE). The physical parameters used in the simulation correspond to the Mambo multi-rotor designed by the French company Parrot and whose values are given in Table 2.

**Table 2** Physical parameters of the mambo multicopter..

Parameter	Description	Units
$m$	Mass	74g
$r$	Propeller radius	3.3 cm

## 4.1 Formal definitions of the benchmarking's controllers

The nonlinear control  $T_{NL}$  is defined by Equation (20) and is obtained by removing the ESO and ground-effect compensation in controller (12).

$$T_{NL} = -\Lambda^{-1}(\phi, \theta) (\sigma_{M_2}(a_1 v_z + \sigma_{M_1}(a_2 v_z + a_1 a_2(z - z_d)))) \quad (20)$$

Motivated by the works in [21, 40], an **in-ground-effect controller** is proposed. This controller includes an IGE ground effect compensator [16] to the nonlinear controller (20). The so obtained  $T_{IGE-NL}$  controller is defined by:

$$T_{IGE-NL} = -\tilde{\Lambda}^{-1}(\phi, \theta, z_r) (\sigma_{M_2}(a_1 v_z + \sigma_{M_1}(a_2 v_z + a_1 a_2(z - z_d)))) \quad (21)$$

The  $T_{IGE-NL}$  controller can keep the aircraft at low altitudes by mitigating ground effects.

The proposed previous ADRC-IGE control algorithm (12) considers the ground effect. In order to compare with a control law without ground effect compensation, let  $T_{ADRC-NL}$  be defined by the following equation, replacing  $\tilde{\Lambda}(\phi, \theta, z_r)$  by  $\Lambda(\phi, \theta)$ :

$$T_{ADRC-NL} = -\Lambda(\phi, \theta) \left( \hat{\xi}_z + \sigma_{M_2}(a_1 v_z + \sigma_{M_1}(a_2 v_z + a_1 a_2(z - z_d))) \right) \quad (22)$$

The modified super twisting sliding mode strategy proposed in [36] has also been chosen in our benchmark since it is known to be efficient under wind disturbances. However, it has to be tested at low altitudes where the ground effect is more significant. The MST-SMC controller is defined by:

$$T_{MST-SMC} = -\Lambda^{-1}(\phi, \theta) \left( g + \ddot{z}_d - \beta_1 \dot{e} - k_1 |s|^{1/2} \text{sign}(s) - k_2 s - k_3 \int_0^t \text{sign}(s) d\tau - k_4 \int_0^t s d\tau \right) \quad (23)$$

## 4.2 Benchmark's scenario

A scenario is conducted, applying successively the five control laws given above. This scenario consists of a take-off phase with a target altitude of 30 cm from  $t = 0$  to  $t = 10$  s. This phase allows the ESO of controllers  $T_{ADRC-NL}$  and  $T_{IGE-ADRC-NL}$  to converge to steady-state behavior. Hence, the performance indexes are computed using only the measurements after  $t = 10$  s to have indexes independent of the initialization of the ESOs. At time  $t = 10$  s a step up to the altitude of 50 cm is applied, followed at  $t = 20$  s by a second one with a target altitude of 70 cm. Finally, two descending steps are applied at  $t = 30$  s with a first low target altitude of 20 cm followed 10 s later with a very low target altitude of 5 cm. This altitude is kept during 20 s until  $t = 60$  s, end of the scenario. In addition, beginning at time  $t = 5$  s, a vertical oscillatory

disturbance is added:

$$\xi_T(t) = A(1 + \exp(-\sin(6\pi f_w t) \sin(2\pi f_w t) \cos(2\pi f_w t))) \quad (24)$$

The frequency range of natural wind gusts is approximately  $0.005\text{ Hz}$  to  $0.14\text{ Hz}$  according to [35, 57], therefore we choose a disturbance frequency  $f_w = 0.1\text{ Hz}$  and a disturbance amplitude  $A = 0.4$ .

### 4.3 Numerical results

Figure 3 shows the aircraft altitude evolution subject to the proposed controller and the controllers described in 4.1. The  $T_{NL}$  and  $T_{IGE-NL}$  controllers stabilize the system near the desired reference. However, both are susceptible to external disturbance. Moreover, the controller  $T_{NL}$  cannot attenuate the ground effect during landing and take-off maneuvers. In contrast, the controller  $T_{IGE-NL}$  compensates for this effect thanks to the incorporation of the in-ground effect model in the control law.

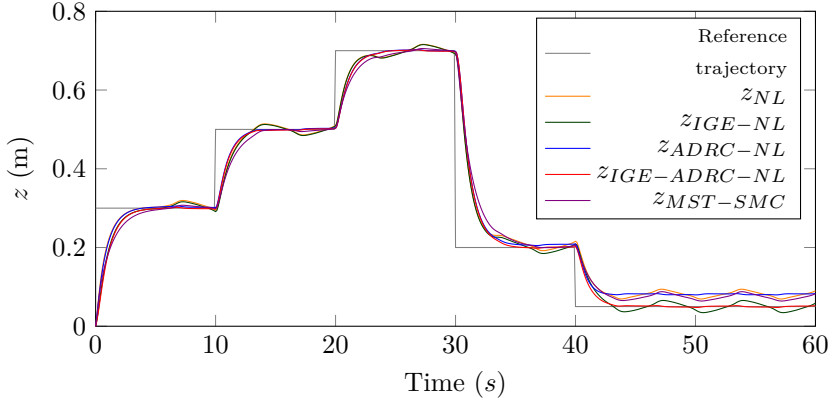
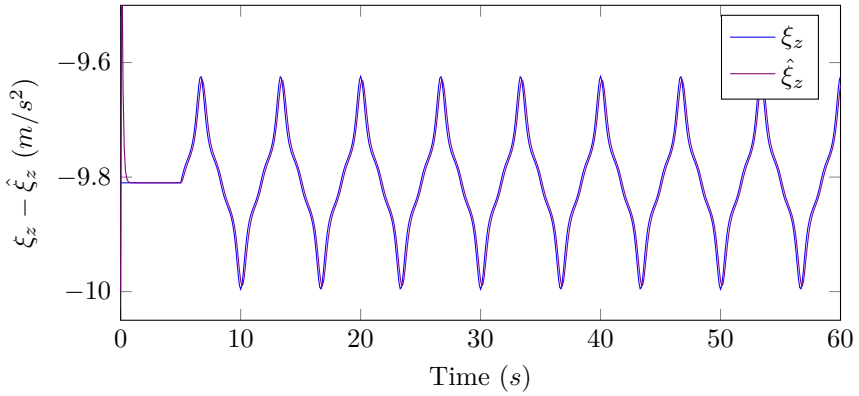
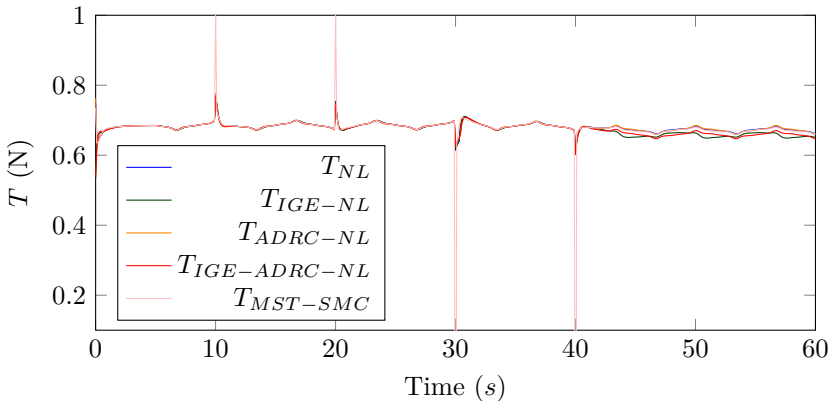
On the other hand, the  $T_{ADRC-NL}$  and  $T_{IGE-ADRC-NL}$  controllers have similar behavior for  $t = 0$  to  $t = 40\text{ s}$ ; both allow estimating online the additive disturbance perfectly (see Figure 4) given by (24) via the ESO and rejecting it through the control law. However, the ground effect in very-low altitude affects the closed-loop system with  $T_{ADRC-NL}$ , as depicted for  $t > 40\text{ s}$ , generating a steady state error of approximately  $5\text{ cm}$  with slight oscillations. This effect is compensated effectively via the controller  $T_{IGE-ADRC-NL}$  thanks to the incorporation of the in-ground effect model in the control law and the ESO, allowing to estimate and compensate for the external additive disturbances given by the wind gust and multiplicative disturbance given by the ground effect during low-altitude flights.

Finally, the modified super twisting sliding mode control  $T_{MST-SMC}$  is evaluated. This controller shows robustness towards the disturbance from wind gusts. However, it needs to be more robust against the ground effect. Note that the low-altitude maneuvers are affected during  $t > 30\text{ s}$ , generating a closed-loop poor performance. Furthermore, unlike the previously described control laws, the control signal's magnitude for the  $T_{MST-SMC}$  becomes very large, which can cause actuators saturation. The evolution of the control signals for the five control strategies is depicted in Figure 5.

As mentioned previously, classical performance indexes are used in all simulations to evaluate the closed-loop performance. Table 3 displays the results obtained for each index. Given these results, the proposed controller presents the slightest error in all the used performance indexes. It is worth noticing that the second better performance is obtained with the controller  $T_{IGE-NL}$ .

**Table 3** Performance index for the flight scenario in the simulation.

Controller	ISE	ITSE	IAE	ITAE
$T_{NL}$	0.253	7.52	1.95	64.95
$T_{IGE-NL}$	0.242	6.89	1.52	43.52
$T_{MST-SMC}$	0.271	7.82	1.89	60.93
$T_{ADRC-NL}$	0.266	7.95	1.83	63.19
$T_{IGE-ADRC-NL}$	0.234	6.54	1.23	33.58

**Fig. 3** Aircraft altitude evolution subject to the different control strategies**Fig. 4** True and estimated disturbance applied to the aircraft during flight

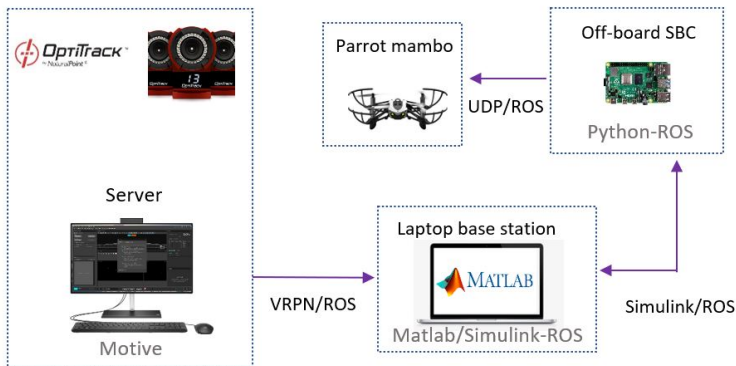


**Fig. 6** General diagram of the experimental platform.

## 5 Experimental Results

The experimental results were generated through a flight arena using a camera-based motion capture system, a communication network for transmitting information through ROS, and various specialized software. The flight arena has an interior space of 22.5 cubic meters, 3 meters long by 3 meters wide, and 2.5 meters high. The flight arena features six Flex 13 cameras with 1280 by 1024 resolution at 120 frames per second, a server, a personal computer dedicated to designing control algorithms, and a Raspberry Pi single-chip computer with communication capabilities with the ROS middleware. The unmanned aerial vehicle used in conjunction with the test bench is the Parrot Mambo. The choice of the vehicle focuses on its small dimensions and its performance for handling indoors. In conjunction with the cameras, the facility allows flights to be carried out in a safe and controlled environment. The OptiTrack system is used for its accuracy at the millimeter level to estimate the pose of any rigid body with six degrees of freedom. Data transmission through a local network is used. The multi-rotor estimation of position, linear velocity, and attitude (quaternion) is sent to a ground station via the VRPN ROS network at 120 Hz. The control algorithm is evaluated at this ground station and sent to a single-board computer via ROS. Finally, the SBC sends the control data to the drone using the same ROS network and UDP packets. Figure 6 shows the general diagram of the experimental platform.

Three scenarios have been considered to evaluate and compare the performance of each controller. For each scenario, different control algorithms have been compared where each algorithm has been repeated five times, and an average of each performance index has been obtained.

## 5.1 Scenario 1: Setpoint regulation at medium and very low altitudes and without external disturbances

This scenario evaluates closed-loop performance for medium and low-altitude flights with significant ground effects and without external disturbances. The take-off maneuver is performed from  $t = 0$  to  $t = 10$  s at a desired setpoint of  $z_d = 0.65$  m. This phase allows the ESO of the  $T_{ADRC-NL}$  and  $T_{IGE-ADRC-NL}$  controllers to converge towards steady-state behavior. Hence, the performance indexes are computed using only the measurements after  $t = 10$  s. Next, the desired reference is set to  $z_d = 0.8$  m in  $t = 10$  to  $t = 20$  s. The ground effect is negligible at this altitude. Then the aircraft flies at low altitudes where the ground effect becomes meaningful; the desired references are  $z_d \in \{0.5, 0.25, 0.14, 0.09\}$  m during  $t = 20$  to  $t = 60$  s.

Figure 7 shows the aircraft altitude evolution subject to the proposed controller and the controllers described in 4.1. The  $T_{NL}$  controller presents an oscillatory response and a steady state error at low altitudes. The  $T_{IGE-NL}$  and  $T_{MST-SMC}$  controllers achieve robustness towards the ground effect up to 0.25 m. However, they fail to attenuate ground effect at very low altitudes, exhibiting oscillatory response and steady-state error; see Figure 7 at  $t > 50$  s. Furthermore, the control effort becomes considerable for  $T_{MST-SMC}$ , especially with the change of reference, take-off, and landing maneuvers. Figure 9 shows the thrust control signals of the different control strategies presented. On the other hand, the  $T_{ADRC-NL}$  and  $T_{IGE-ADRC-NL}$  controllers work desirably; the estimated total disturbance obtained via the ESO is depicted in Figure 8. Note that this disturbance contains gravity acceleration and additive disturbances from the environment. However, the  $T_{IGE-ADRC-NL}$  performs better following the desired reference and a fast stabilization and does not present an oscillatory response at very low altitudes or error in the steady state. Table 4 displays the results obtained for each performance index. It can be seen that the proposed controller presents the slightest error. A video performing the flights described in this scenario is shown in the following link: <https://drive.google.com/file/d/1Lbv8drj7K3Bh3XQOLQcVXxyR4UEidhhM/view?usp=sharing>

**Table 4** Performance index for scenario 1

Controller	ISE	ITSE	IAE	ITAE
$T_{NL}$	2.35	16.03	4.14	76.25
$T_{IGE-NL}$	2.06	15.79	4.08	74.51
$T_{MST-SMC}$	1.83	14.91	3.71	68.35
$T_{ADRC-NL}$	1.69	12.81	3.17	63.19
$T_{IGE-ADRC-NL}$	1.61	12.42	3.04	61.15

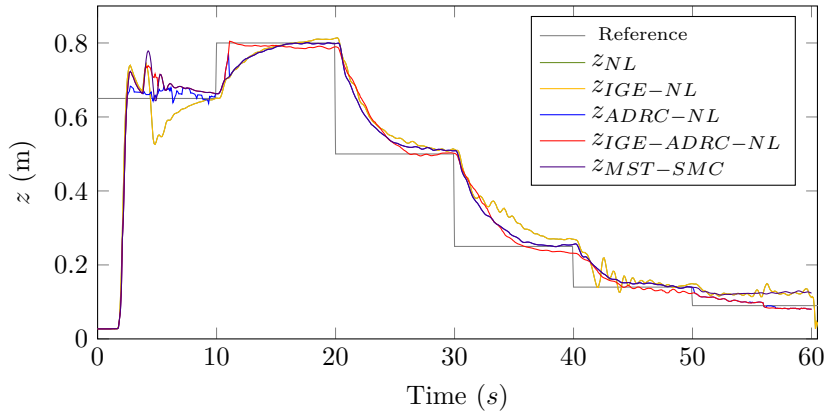


**Fig. 7** Scenario 1: Aircraft altitude evolution subject to the different control strategies

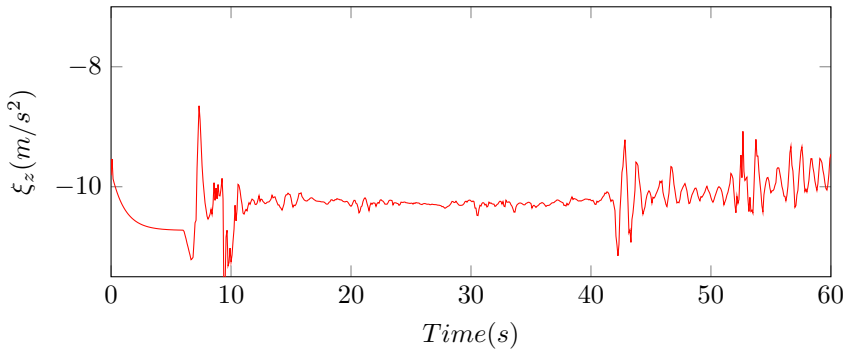


**Fig. 8** Scenario 1: Estimated disturbance  $\tilde{\xi}_z(t)$ .

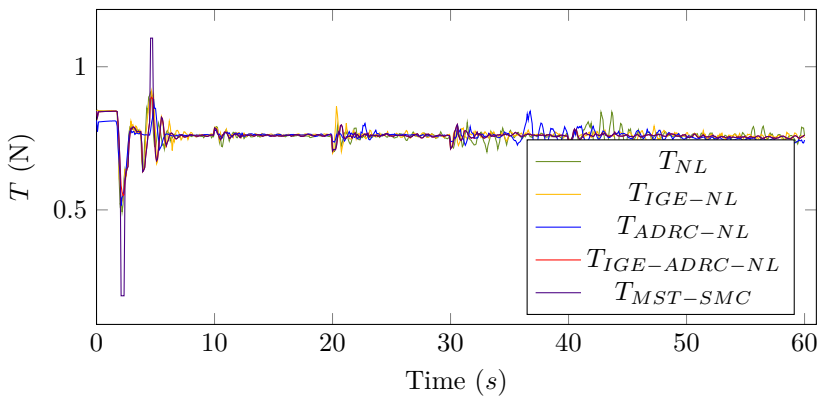


**Fig. 9** Scenario 1: Aircraft control signal evolution subject to the different control strategies

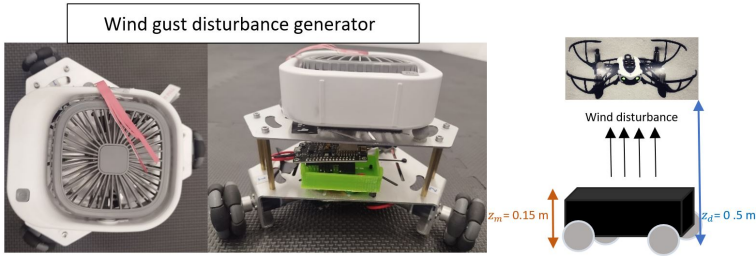


**Fig. 10** Wind gust disturbance generator.

## 5.2 Scenario 2: Setpoint regulation at medium altitude and with external disturbances.

In this scenario, the aircraft's closed-loop behavior is investigated when influenced by ground effect and wind gust disturbance. Figure 10 shows the benchmark implemented to accomplish this task. It consists of an omnidirectional mobile robot and a fan on its surface. The mobile robot's movement is programmed to go forward and backward periodically, emulating a sinusoidal wind gust disturbance. The wind speed generated by the fan is 11 m/s.

The flight is conducted at a medium altitude of 0.5 m. Then the ground effect is generated when the mobile robot coincides with the aircraft's position, where the vertical distance between the aircraft and the mobile robot is 0.25 m.

The take-off maneuver is performed from  $t = 0$  to  $t = 13$  s at a desired setpoint of  $z_d = 0.65$  m. This phase allows the ESO of the  $T_{ADRC-NL}$  and  $T_{IGE-ADRC-NL}$  controllers to converge to a steady-state behavior. Hence, the performance indexes are computed using only the measurements after  $t = 13$  s. Next, the desired reference is set to  $z_d = 0.8$  m from  $t = 15$  to  $t = 25$  s. The ground effect is negligible at this altitude; nevertheless, the disturbance is presented, which is estimated via the ESO whose evolution is depicted in Figure 12. Finally, the desired reference is set to  $z_d = 0.5$  (distance relative of 0.25 m between the aircraft and the mobile robot when they coincide).

According to Figure 11, where the aircraft's evolution altitude is depicted, the  $T_{NL}$  and  $T_{IGE-NL}$  controllers are susceptible to the disturbance generated by the wind and the ground effect when the mobile robot approaches the aircraft. With  $T_{NL}$ , the closed-loop performance is degraded at  $t = 20$  s and  $t = 30$ , presenting a more significant oscillation. The  $T_{MST-SMC}$  shows better behavior than the previous ones. However, it still presents an oscillatory response to low altitudes, as seen for  $t > 25$  s. Furthermore, its control signal presents slight chattering, as seen in Figure 13. The  $T_{ADRC-NL}$  controller can estimate both disturbances, due to the high degree of convergence and the wide frequency bandwidth of the ESO; however, since the ground effect is a multiplicative disturbance, offset and oscillation are shown for take-off maneuver. On the other hand, it shows good behavior when dealing with

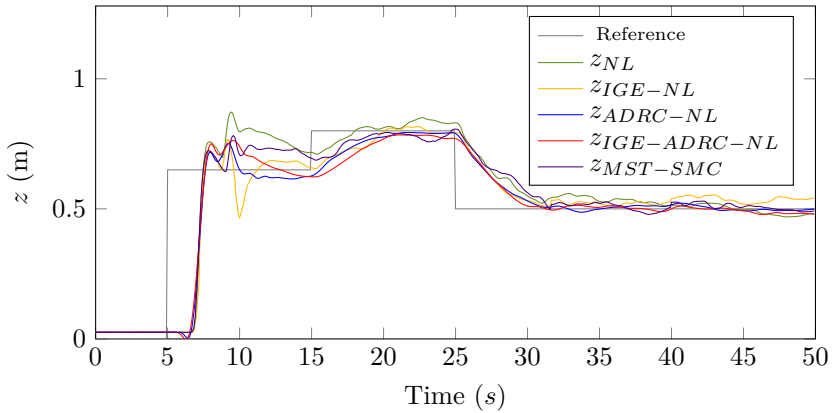


**Fig. 11** Scenario 2: Aircraft altitude evolution subject to the different control strategies

the wind disturbance. Finally, the one that shows the best behavior is the  $T_{IGE-ADRC-NL}$  controller since the IGE compensates the gain of the multiplicative disturbance, counteracting the insufficient disturbance compensation capacity of the ADRC. Both present a smooth response and excellent stabilization. Table 5 displays the results obtained for each performance index. It can still be noticed that the proposed controller presents the slightest error. A video performing the flights described in this scenario is shown in the following link: <https://drive.google.com/file/d/1OktoFYDQ3k7csLRhxPiKAbQMIEfyWbKH/view?usp=sharing>

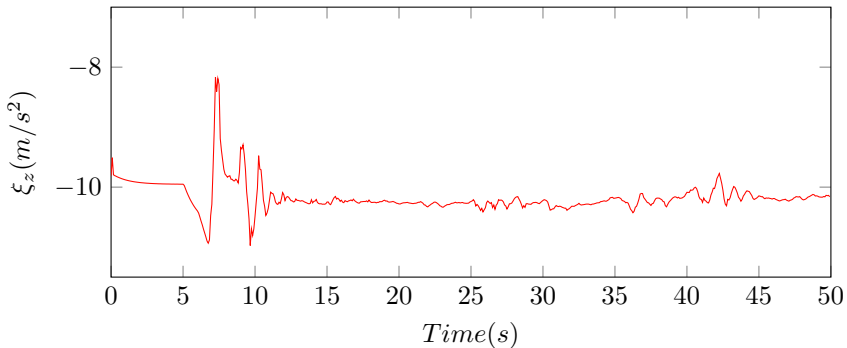


**Fig. 12** Scenario 2: Estimated disturbance  $\tilde{\xi}_z(t)$ .

### 5.3 Scenario 3: Trajectory tracking at low altitude.

In this scenario, we address the trajectory tracking problem at low altitudes. The chosen trajectory is the sinusoidal signal  $z_d(t) = 0.25 - 0.1 \cos(0.35t)$ . Although the proposed control algorithm and those presented in 4.1 are

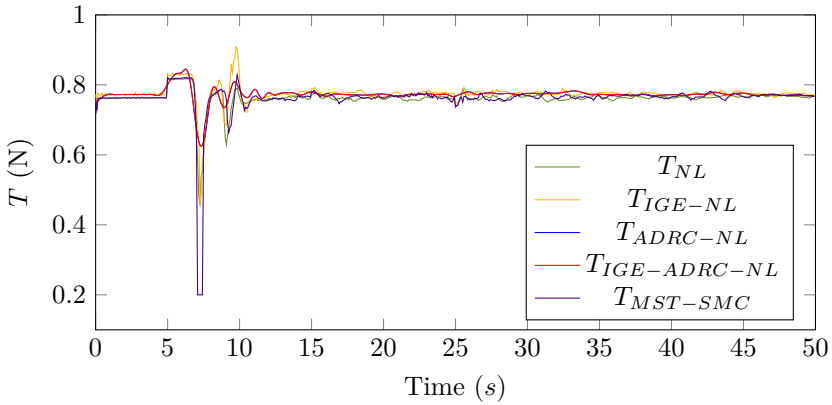


**Fig. 13** Scenario 2: Aircraft control signal evolution subject to the different control strategies

**Table 5** Performance index for scenario 2

Controller	ISE	ITSE	IAE	ITAE
$T_{NL}$	3.90	28.85	9.47	127.02
$T_{IGE-NL}$	3.66	26.43	8.21	108.91
$T_{MST-SMC}$	3.21	24.52	7.42	97.63
$T_{ADRC-NL}$	2.35	18.27	6.48	81.94
$T_{IGE-ADRC-NL}$	1.82	9.55	5.59	79.23

designed for regulation purposes (except the  $T_{MST-SMC}$ ), they perform well following the desired low-frequency reference. As shown in Figure 14, the aircraft performs the take-off maneuver from  $t = 0$  to  $t = 10$  s, followed by the reference tracking. Note that the minimum desired altitude is 0.15 m, enough to experience the ground effect.

The  $T_{NL}$ ,  $T_{IGE-NL}$  and  $T_{MST-SMC}$  controllers present a considerable oscillation in the take-off maneuver and a lag in trajectory following, in addition to having an oscillatory behavior and error when the reference reaches its minimum value (0.15 m) due to the ground effect. The  $T_{ADRC-NL}$  controller presents a smooth response; it is robust against additive disturbances but fails when dealing with multiplicative disturbances such as the ground effect presenting a steady-state error.

On the other hand, the closed-loop system with the proposed controller  $T_{IGE-ADRC-NL}$  makes it possible to compensate for multiplicative disturbances such as the ground effect and is robust against additive disturbances and modeling uncertainties, which is estimated via the ESO and depicted in Figure 15. Its response is smooth; it always follows the reference, even at minimum altitude, where the ground effect becomes significant. The control signal evolution is depicted in Figure 16. Table 6 displays the results obtained for each performance index. Once again, the proposed controller presents the slightest error.

A video performing the flights described in this scenario is shown in the following link: [https://drive.google.com/file/d/1xuLlv07Zic0BdEUoHPyvwfnPfl\\_QjL8\\_/view?usp=sharing](https://drive.google.com/file/d/1xuLlv07Zic0BdEUoHPyvwfnPfl_QjL8_/view?usp=sharing)

**Table 6** Performance index for scenario 3

Controller	ISE	ITSE	IAE	ITAE
$T_{NL}$	5.81	31.85	10.47	131.19
$T_{IGE-NL}$	4.76	29.59	9.30	120.09
$T_{MST-SMC}$	4.67	26.42	9.21	118.63
$T_{ADRC-NL}$	3.19	21.10	6.48	98.51
$T_{IGE-ADRC-NL}$	3.02	20.87	6.12	95.22

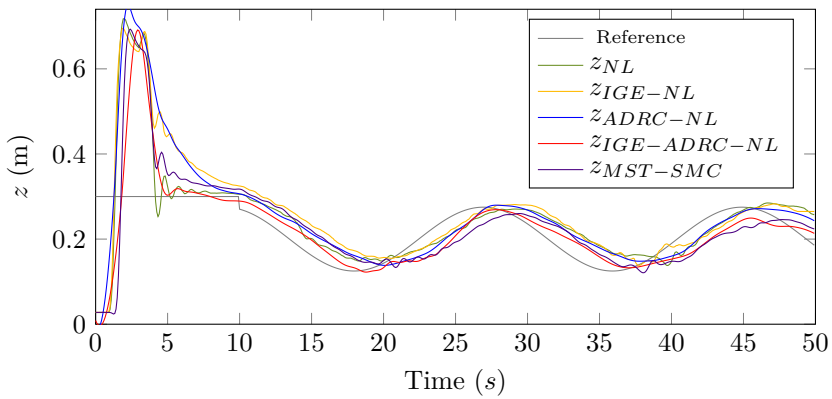


**Fig. 14** Scenario 3: Aircraft altitude evolution subject to the different control strategies

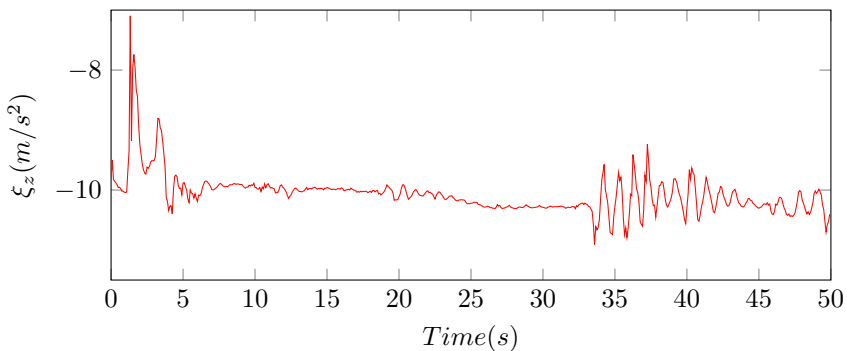


**Fig. 15** Scenario 3: Estimated disturbance  $\tilde{\xi}_z(t)$ .

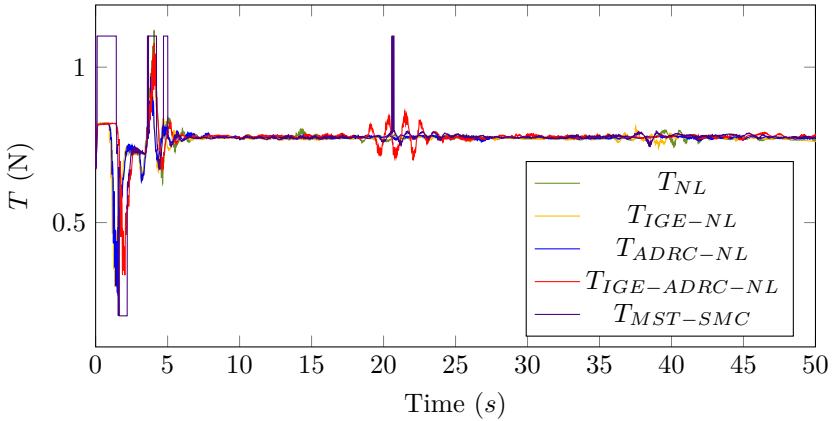


**Fig. 16** Experimental result: Aircraft control signal evolution subject to the different control strategies

## 6 Conclusion

This paper presented a control strategy combining the advantages of the ADRC philosophy using an ESO to estimate the total additive disturbance, a smooth nonlinear feedback control based on inner saturation functions, and a mathematical model characterizing the ground effect on low-altitude flights dealing with the multiplicative disturbance. Theoretical, simulation, and experimental results were obtained throughout this research. Furthermore, a set of control scenarios has been defined to evaluate the proposed strategy's advantages. It has been compared to a well-established robust nonlinear controller, the Modified Super Twisting Sliding Mode Controller (MST-SMC). Comparative results for ISE, ITSE, IAE, and ITAE performance indexes show that the proposed  $T_{IGE-ADRC-NL}$  controller overcomes all the controller scenarios, including the MST-SMC. Due to its relative simplicity, the control algorithm is easy to implement, the control signal is smooth, not suffering from the chattering effect, and the closed-loop stability is guaranteed. In the future, an algorithm using AI techniques will be proposed to adjust the ground effect compensation online and the ESO's gains by detecting landing zones. In addition, an extension of the trajectory-tracking problem in the 2D to low altitude will be formulated.

## Appendix A Identification of the correction factor in the ground effect model

Some experiments were conducted to determine the correction factor in the ground effect model described in [16]. The ground effect is a function of the radius of the rotor  $r$  and the vertical distance from the rotor to the ground denoted  $z_r$  as described in the expression (A1), where  $T_{input}$  is the input

thrust commanded by the flight controller and  $T_{output}$  is the actually thrust generated by the aircraft's actuators.

$$\frac{T_{output}}{T_{input}} = \frac{1}{1 - \rho \left( \frac{r}{4z_r} \right)^2} \quad (\text{A1})$$

In conditions with a ground effect, a greater thrust  $T_{output}$  will be produced than  $T_{input}$ . At hover, ideally,  $T_{input} = mg$  is constant [17], then, producing flights at low desired altitudes given by  $z_d \in \{0.05, 0.1, 0.15, 0.2, 0.25, 0.3, 0.35, 0.4, 0.45, 0.5, 0.55\}$  m, and using least square approximation, we obtain the graph described in Figure A1. The solid curve is the fitted curve using the least squares approximation, and the square markers (in red) represent the data obtained in our experiments. It is worth mentioning that the controller used for these experiments is the  $T_{NL}$  introduced in 4.1. The correction coefficient calculated with the recorded data was  $\rho = 1.9$ . In [16], the coefficient was identified as  $\rho = 8.6$  and in [17], the coefficient was identified as  $\rho = 3.4$ . This difference can depend on the environment and used aircraft.

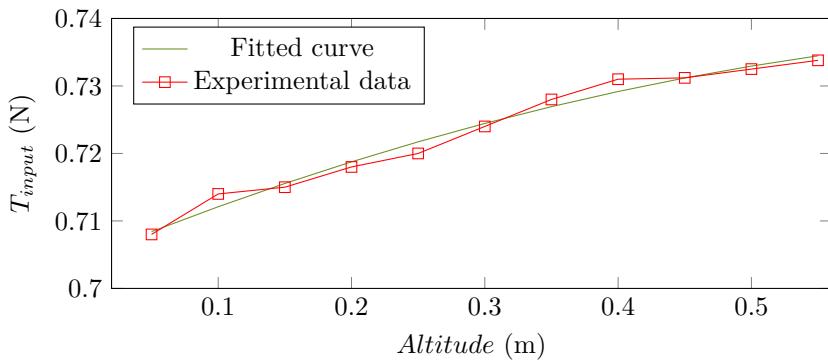


**Fig. A1** Evaluation of Danjun [16] model: thrust vs altitude

In Figure A2 one depicts the ratio of  $T_{output}/T_{input}$  against  $z_r/r$ . From this Figure, one can see that the ground effect slightly influences the aircraft from the height of  $z_r/r = 6$ , *i.e.*,  $z_r = 0.198$  m for the Mambo's propeller radius  $r = 0.033$  m. We assume that this is due to the protective shield of the propellers, which the Mambo drone has.

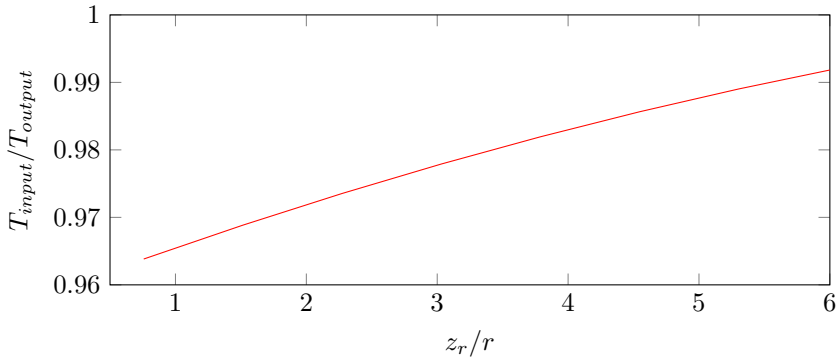


**Fig. A2** Evaluation of Danjun [16] model:  $T_{input}/T_{output}$  Vs  $z_r/r$

## Appendix B Comparative of Existing Ground Effect Model

The different ground effect models introduced in Table 1 were evaluated. Three desired low-altitudes, where the ground effect takes place, have been considered;  $z_d \in \{0.25, 0.15, 0.05\}$  m. The  $T_{NL}$  controller is used for all experiments. The ground effect models are incorporated into the ESO and the  $T_{IGE-ADRC-NL}$  controller to be fair in the comparisons. Figure B3 shows the altitude's evolution. As is already known, the Cheeseman model does not accurately describe the disturbance generated by the ground effect in multi-rotors. The model proposed by Hayden improves the previous one. However, it still has errors in stabilization at low altitudes. Besides, the Danjun and Kan models show higher performance at low altitudes. Since the Kan model is designed for forward flight, it incorporates the knowledge of velocity  $V$ . Therefore, it is preferred to use the Danjun model for hover scenarios. The Kan model will be used for navigation and trajectory-tracking applications in future work. Table 6 displays the results obtained for each performance index. Note that the slightest error is obtained for Dnajun's model, followed by Kan's model.

**Table B1** Performance index Ground-Effect models.

Models	ISE	ITSE	IAE	ITAE
Cheeseman	2.9	21.23	7.12	80.16
Hayden	2.75	19.93	6.22	77.26
Dnajun	2.54	17.08	5.44	71.39
Kan	2.61	17.12	5.68	70.01

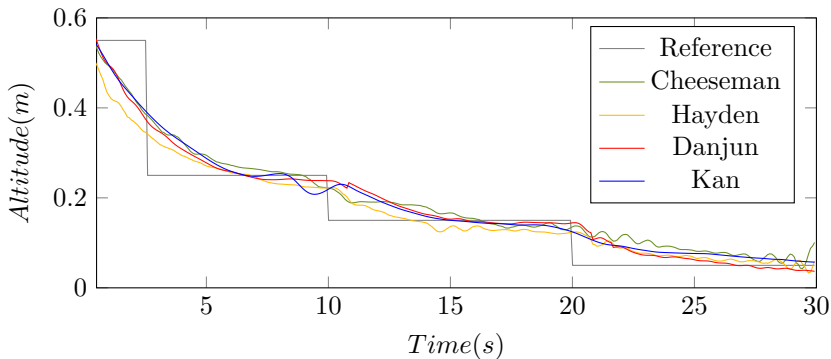


**Fig. B3** Comparative of Ground Effect Model.

**Author Contributions.** Conceptualization: J. Díaz-Téllez and J.F. Guerrero-Castellanos; Methodology: J.F. Guerrero-Castellanos, N. Marchand and S. Durand; Software and analysis: J. Díaz-Téllez and F. Pouthier; Writing - original draft preparation: J. Díaz-Téllez and J.F. Guerrero-Castellanos; Writing - review and editing: N. Marchand, F. Pouthier, S. Durand.

**Acknowledgements.** J. Díaz-Téllez thanks the National Council of Science and Technology, Mexico (CONACYT) for providing financial support through his Ph. D. scholarship.

**Funding.** This work is part of the French-Mexican TOBACCO project funded by the FORDECYT-PRONACES through the joint SEP-CONACYT-ANUIES-ECOS Nord program (MX-296702 & FR-M18M02).

**Data Availability.** The data sets generated and analyzed during the current study are available from the corresponding author on reasonable request.

## Declarations

**Conflicts of interest** The authors declare no conflict of interest.

**Ethics Approval** Research does not involve Human Participants and/ or Animals.

**Consent to participate** Not applicable.

**Consent to publish** Not applicable.

## References

- [1] He, T., Zeng, Y., Hu, Z.: Research of multi-rotor uavs detailed autonomous inspection technology of transmission lines based on route planning. *IEEE Access* **7**, 114955–114965 (2019). <https://doi.org/10.1109/ACCESS.2019.2935551>

- [2] Chung, H.-M., Maharjan, S., Zhang, Y., Eliassen, F., Strunz, K.: Placement and routing optimization for automated inspection with unmanned aerial vehicles: A study in offshore wind farm. *IEEE Transactions on Industrial Informatics* **17**(5), 3032–3043 (2021). <https://doi.org/10.1109/TII.2020.3004816>
- [3] Sawadstitang, S., Niyato, D., Tan, P.-S., Wang, P.: Joint ground and aerial package delivery services: A stochastic optimization approach. *IEEE Transactions on Intelligent Transportation Systems* **20**(6), 2241–2254 (2019). <https://doi.org/10.1109/TITS.2018.2865893>
- [4] Tokekar, P., Hook, J.V., Mulla, D., Isler, V.: Sensor planning for a symbiotic uav and ugv system for precision agriculture. *IEEE Transactions on Robotics* **32**(6), 1498–1511 (2016). <https://doi.org/10.1109/TRO.2016.2603528>
- [5] Reddy Maddikunta, P.K., Hakak, S., Alazab, M., Bhattacharya, S., Gadekallu, T.R., Khan, W.Z., Pham, Q.-V.: Unmanned aerial vehicles in smart agriculture: Applications, requirements, and challenges. *IEEE Sensors Journal* **21**(16), 17608–17619 (2021). <https://doi.org/10.1109/JSEN.2021.3049471>
- [6] Zhang, S., Xue, X., Chen, C., Sun, Z., Sun, T.: Development of a low-cost quadrotor uav based on adrc for agricultural remote sensing. *International Journal of Agricultural and Biological Engineering* **12**, 82–87 (2019). <https://doi.org/10.25165/j.ijabe.20191204.4641>
- [7] Chhikara, P., Tekchandani, R., Kumar, N., Guizani, M., Hassan, M.M.: Federated learning and autonomous uavs for hazardous zone detection and aqi prediction in iot environment. *IEEE Internet of Things Journal* **8**(20), 15456–15467 (2021). <https://doi.org/10.1109/JIOT.2021.3074523>
- [8] Lu, Y., Macias, D., Dean, Z.S., Kreger, N.R., Wong\*, P.K.: A uav-mounted whole cell biosensor system for environmental monitoring applications. *IEEE Transactions on NanoBioscience* **14**(8), 811–817 (2015). <https://doi.org/10.1109/TNB.2015.2478481>
- [9] Sambolek, S., Ivasic-Kos, M.: Automatic person detection in search and rescue operations using deep cnn detectors. *IEEE Access* **9**, 37905–37922 (2021). <https://doi.org/10.1109/ACCESS.2021.3063681>
- [10] Dousai, N.M.K., Lončarić, S.: Detecting humans in search and rescue operations based on ensemble learning. *IEEE Access* **10**, 26481–26492 (2022). <https://doi.org/10.1109/ACCESS.2022.3156903>
- [11] Nascimento, T.P., Saska, M.: Position and attitude control of multi-rotor aerial vehicles: A survey. *Annual Reviews in Control* **48**, 129–146 (2019).

<https://doi.org/10.1016/j.arcontrol.2019.08.004>

- [12] Abdelmaksoud, S.I., Mailah, M., Abdallah, A.M.: Control strategies and novel techniques for autonomous rotorcraft unmanned aerial vehicles: A review. *IEEE Access* **8**, 195142–195169 (2020). <https://doi.org/10.1109/ACCESS.2020.3031326>
- [13] González-Guerrero, J.C., Díaz-Téllez, J., Estevez-Carreón, J., Mendoza-Vázquez, R., Meraz-Melo, M.A., Guerrero-Castellanos, J.F.: Low altitude control of the vtol uav tolerant to ground effect and actuator failures. In: 2022 International Conference on Unmanned Aircraft Systems (ICUAS), pp. 1504–1509 (2022). <https://doi.org/10.1109/ICUAS54217.2022.9836161>
- [14] Cheeseman, I.C., D, P., Bennett, W.E., D, P., Bennett, W.E.: The effect of ground on a helicopter rotor in forward flight. Technical report (1955)
- [15] Hayden, J.S.: The effect of the ground on helicopter hovering power required. (1976)
- [16] Danjun, L., Yan, Z., Zongying, S., Geng, L.: Autonomous landing of quadrotor based on ground effect modelling. In: 2015 34th Chinese Control Conference (CCC), pp. 5647–5652 (2015). <https://doi.org/10.1109/ChiCC.2015.7260521>
- [17] Kan, X., Thomas, J., Teng, H., Tanner, H.G., Kumar, V., Karydis, K.: Analysis of ground effect for small-scale uavs in forward flight. *IEEE Robotics and Automation Letters* **4**(4), 3860–3867 (2019). <https://doi.org/10.1109/LRA.2019.2929993>
- [18] Sharf, I., Nahon, M., Harmat, A., Khan, W., Michini, M., Speal, N., Trentini, M., Tsadok, T., Wang, T.: Ground effect experiments and model validation with draganflyer x8 rotorcraft. In: 2014 International Conference on Unmanned Aircraft Systems (ICUAS), pp. 1158–1166 (2014). <https://doi.org/10.1109/ICUAS.2014.6842370>
- [19] Ryan, T.: Modelling of quadrotor ground effect forces via simple visual feedback and support vector regression. (2012). <https://doi.org/10.2514/6.2012-4833>
- [20] Davis, E., Pounds, P.E.I.: Passive position control of a quadrotor with ground effect interaction. *IEEE Robotics and Automation Letters* **1**(1), 539–545 (2016). <https://doi.org/10.1109/LRA.2016.2514351>
- [21] Anh, T.H., Binh, N.T., Song, J.W.: In-ground-effect model based adaptive altitude control of rotorcraft unmanned aerial vehicles. *IEEE Robotics and Automation Letters* **7**(2), 794–801 (2022). <https://doi.org/10.1109/>

[LRA.2021.3133932](#)

- [22] Castillo, P., Dzul, A., Lozano, R.: Real-time stabilization and tracking of a four-rotor mini rotorcraft. *IEEE Transactions on Control Systems Technology* **12**(4), 510–516 (2004). <https://doi.org/10.1109/TCST.2004.825052>
- [23] Lee, T., Leok, M., McClamroch, N.H.: Geometric tracking control of a quadrotor uav on  $se(3)$ . In: 49th IEEE Conference on Decision and Control (CDC), pp. 5420–5425 (2010). <https://doi.org/10.1109/CDC.2010.5717652>
- [24] González, I., Salazar, S., Lozano, R.: Chattering-free sliding mode altitude control for a quad-rotor aircraft: Real-time application. In: *Journal of Intelligent & Robotic Systems*, pp. 137–155 (2014). <https://doi.org/10.1007/s10846-013-9913-8>
- [25] Muñoz, F., González-Hernández, I., Salazar, S., Espinoza, E.S., Lozano, R.: Second order sliding mode controllers for altitude control of a quadrotor uas: Real-time implementation in outdoor environments. *Neurocomputing* **233**, 61–71 (2017). <https://doi.org/10.1016/j.neucom.2016.08.111>. SI: CCE 2015
- [26] Xuan Mung, N., Hong, S.-K.: Improved altitude control algorithm for quadcopter unmanned aerial vehicles. *Applied Sciences* **9** (2019). <https://doi.org/10.3390/app9102122>
- [27] Ahmed, N., Raza, A., Shah, S.A.A., Khan, R.: Robust composite-disturbance observer based flight control of quadrotor attitude. *Journal of Intelligent & Robotic Systems* **103**(1) (2021). <https://doi.org/10.1007/s10846-021-01463-6>
- [28] Younes, Y., Drak, A., Noura, H., Rabhi, A., El hajjaji, A.: Robust model-free control applied to a quadrotor uav. *Journal of Intelligent & Robotic Systems* **84** (2016). <https://doi.org/10.1007/s10846-016-0351-2>
- [29] Kothari, M., Postlethwaite, I., Gu, D.-W.: Uav path following in windy urban environments. *Journal of Intelligent & Robotic Systems* **74**, 1013–1028 (2013). <https://doi.org/10.1007/s10846-013-9873-z>
- [30] Madruga, S.P., Tavares, A.H.B.M., Luiz, S.O.D., do Nascimento, T.P., Lima, A.M.N.: Aerodynamic effects compensation on multi-rotor uavs based on a neural network control allocation approach. *IEEE/CAA Journal of Automatica Sinica* **9**(2), 295–312 (2022). <https://doi.org/10.1109/JAS.2021.1004266>
- [31] Hedjar, R., Al Zuair, M.A.: Robust altitude stabilization of vtol-uav for

- payloads delivery. *IEEE Access* **7**, 73583–73592 (2019). <https://doi.org/10.1109/ACCESS.2019.2919701>
- [32] Kazim, M., Azar, A.T., Koubaa, A., Zaidi, A.: Disturbance-rejection-based optimized robust adaptive controllers for uavs. *IEEE Systems Journal* **15**(2), 3097–3108 (2021). <https://doi.org/10.1109/JSYST.2020.3006059>
- [33] Cabecinhas, D., Cunha, R., Silvestre, C.: A globally stabilizing path following controller for rotorcraft with wind disturbance rejection. *IEEE Transactions on Control Systems Technology* **23**(2), 708–714 (2015). <https://doi.org/10.1109/TCST.2014.2326820>
- [34] Azid, S.I., Kumar, K., Cirrincione, M., Fagiolini, A.: Robust motion control of nonlinear quadrotor model with wind disturbance observer. *IEEE Access* **9**, 149164–149175 (2021). <https://doi.org/10.1109/ACCESS.2021.3124609>
- [35] Asignacion, A., Suzuki, S., Noda, R., Nakata, T., Liu, H.: Frequency-based wind gust estimation for quadrotors using a nonlinear disturbance observer. *IEEE Robotics and Automation Letters* **7**(4), 9224–9231 (2022). <https://doi.org/10.1109/LRA.2022.3190073>
- [36] Muñoz, F., González-Hernández, I., Salazar, S., Espinoza, E.S., Lozano, R.: Second order sliding mode controllers for altitude control of a quadrotor uas: Real-time implementation in outdoor environments. *Neurocomputing* **233**, 61–71 (2017). <https://doi.org/10.1016/j.neucom.2016.08.111>. SI: CCE 2015
- [37] Shtessel, Y., Edwards, C., Fridman, L., Levant, A.: *Sliding Mode Control and Observation*. Birkhäuser New York, NY, ??? (2014)
- [38] Chen, Y., Zhang, G., Zhuang, Y., Hu, H.: Autonomous flight control for multi-rotor uavs flying at low altitude. *IEEE Access* **7**, 42614–42625 (2019). <https://doi.org/10.1109/ACCESS.2019.2908205>
- [39] Guo, K., Zhang, W., Zhu, Y., Jia, J., Yu, X., Zhang, Y.: Safety control for quadrotor uav against ground effect and blade damage. *IEEE Transactions on Industrial Electronics* **69**(12), 13373–13383 (2022). <https://doi.org/10.1109/TIE.2022.3140494>
- [40] He, X., Kou, G., Calaf, M., Leang, K.: In-ground-effect modeling and nonlinear disturbance observer for multi-rotor uav control. *Journal of Dynamic Systems, Measurement, and Control* **141** (2019). <https://doi.org/10.1115/1.4043221>

- [41] Han, J.: From PID to active disturbance rejection control. *IEEE Transactions on Industry Electronics* **56**(3), 900–906 (2009)
- [42] Chan, L., Naghdy, F., Stirling, D.: Extended active observer for force estimation and disturbance rejection of robotic manipulators. *Robotics and Autonomous Systems* **61**(12), 1277–1287 (2013)
- [43] Xue, W., Huang, Y., Gao, Z.: On adrc for non-minimum phase systems: canonical form selection and stability conditions. *Control Theory and Technology* **14**(3), 199–208 (2016)
- [44] Mehdi, H., Boubaker, O.: Robust impedance control-based lyapunov-hamiltonian approach for constrained robots. *International Journal of Advanced Robotic Systems* **12**(12), 190 (2015)
- [45] Yu, Y., Yang, Z., Han, C., Liu, H.: Disturbance-observer based control for magnetically suspended wheel with synchronous noise. *Control Engineering Practice* **72**, 83–89 (2018)
- [46] Sira-Ramirez, H., Luviano-Juárez, A., Ramirez-Neria, M., Zurita-Bustamante, E.: Active Disturbance Rejection Control of Dynamic Systems: A Flatness Based Approach, (2018)
- [47] Guo, L., Cao, S.: Anti-disturbance control theory for systems with multiple disturbances: A survey. *ISA Transactions* **53**(4), 846–849 (2014). <https://doi.org/10.1016/j.isatra.2013.10.005>. Disturbance Estimation and Mitigation
- [48] Chang, K., Xia, Y., Huang, K., Ma, D.: Obstacle avoidance and active disturbance rejection control for a quadrotor. *Neurocomputing* **190**, 60–69 (2016). <https://doi.org/10.1016/j.neucom.2016.01.033>
- [49] Dong, W., Gu, G.-Y., Zhu, X., Ding, H.: A high-performance flight control approach for quadrotors using a modified active disturbance rejection technique. *Robotics and Autonomous Systems* **83**, 177–187 (2016). <https://doi.org/10.1016/j.robot.2016.05.005>
- [50] Abadi, A., Amraoui, A.E., Mekki, H., Ramdani, N.: Robust tracking control of quadrotor based on flatness and active disturbance rejection control. *IET Control Theory & Applications* **14**(8), 1057–1068 (2020) <https://arxiv.org/abs/https://ietresearch.onlinelibrary.wiley.com/doi/pdf/10.1049/iet-cta.2019.1363>. <https://doi.org/10.1049/iet-cta.2019.1363>
- [51] Najm, A.A., Ibraheem, I.K.: Altitude and attitude stabilization of uav quadrotor system using improved active disturbance rejection control. *Arabian Journal for Science and Engineering* **45**(3), 1985–1999 (2020).

<https://doi.org/10.1007/s13369-020-04355-3>

- [52] Cheng, Y., Dai, L., Li, A., Yuan, Y., Chen, Z.: Active disturbance rejection generalized predictive control of a quadrotor uav via quantitative feedback theory. *IEEE Access* **10**, 37912–37923 (2022). <https://doi.org/10.1109/ACCESS.2022.3165093>
- [53] Zhang, Y., Chen, Z., Sun, M., Zhang, X.: Trajectory tracking control of a quadrotor uav based on sliding mode active disturbance rejection control. *Nonlinear Analysis: Modelling and Control* **24**(4), 545–560 (2019). <https://doi.org/10.15388/NA.2019.4.4>
- [54] Nie, Z.-Y., Zhang, B., Wang, Q.-G., Liu, R.-J., Luo, J.-L.: Adaptive active disturbance rejection control guaranteeing uniformly ultimate boundedness and simplicity. *International Journal of Robust and Nonlinear Control* **30**(17), 7278–7294 (2020) <https://arxiv.org/abs/https://onlinelibrary.wiley.com/doi/pdf/10.1002/rnc.5177>. <https://doi.org/10.1002/rnc.5177>
- [55] Guerrero-Castellanos, J.F., Rifaï, H., Arnez-Paniagua, V., Linares-Flores, J., Saynes-Torres, L., Mohammed, S.: Robust active disturbance rejection control via control lyapunov functions: Application to actuated-ankle-foot-orthosis. *Control Engineering Practice* **80**, 49–60 (2018)
- [56] Guerrero-Castellanos, J.F., Marchand, N., Hably, A., Lesecq, S., Delamare, J.: Bounded attitude control of rigid bodies: Real-time experimentation to a quadrotor mini-helicopter. *Control Engineering Practice* **19**(8), 790–797 (2011). <https://doi.org/10.1016/j.conengprac.2011.04.004>
- [57] Tomić, T., Haddadin, S.: Simultaneous estimation of aerodynamic and contact forces in flying robots: Applications to metric wind estimation and collision detection. In: 2015 IEEE International Conference on Robotics and Automation (ICRA), pp. 5290–5296 (2015). <https://doi.org/10.1109/ICRA.2015.7139937>